Nanoscale

PAPER

View Article Online
View Journal | View Issue

Cite this: *Nanoscale*, 2025, **17**, 8599

The true atomistic structure of a disordered crystal: a computational study on the photon upconverting material β-$NaYF_4$ and its Er^{3+}-, Tm^{3+}-, and Yb^{3+}-doped derivates†

Chris Steve Conrad, [a,b] Holger Euchner, [a] Eva Hemmer *[b] and Reinhold F. Fink *[a]

Hexagonal (β-) $NaYF_4$ and $LiYF_4$ doped with trivalent lanthanide ions (Ln^{3+}, *e.g.*, Er^{3+}, Tm^{3+}, and Yb^{3+}) are well-known photon upconverting materials. This property is crucially determined by the precise location of the Ln^{3+} dopant ions and their closest neighbouring ions in the host material. However, due to the inherent disorder of the crystal structures the atomistic structure of a disordered crystal such as β-$NaYF_4$ is not unambiguously provided by X-ray diffraction techniques. Here, theoretical estimates for the true structure of the material are obtained *via* periodic density functional theory (DFT) calculations of large supercells. Our results reveal that Ln^{3+} doping of β-$NaYF_4$ occurs in a variety of low-symmetry sites, which are significantly altered by the occupational disorder of the crystal structure. Mainly, the distribution of Na^+ and Y^{3+} around a doping site significantly influences the positions of the F^- closest to the dopant. The results of this study are substantiated by applying the same method on the well-ordered host crystal $LiYF_4$ and by comparison with available experimental and theoretical data. Similar results are expected for other disordered crystalline host materials such as β-$NaGdF_4$ or cubic (α-) $NaYF_4$. The obtained structural information is a prerequisite for future accurate simulations and prediction of key parameters for the upconversion process in bulk materials and nanoparticles.

Received 20th November 2024,
Accepted 14th February 2025

DOI: 10.1039/d4nr04880f

rsc.li/nanoscale

Introduction

Photon upconversion is a process during which the energy of two or more photons of lower energy (typically in the near-infrared, NIR) is captured in a sequential manner to trigger the emission of one single photon of higher energy (in the ultraviolet, visible, or shorter-wavelength NIR regions). The process was first observed in bulk materials but later also transferred to nanomaterials.[1–3] Nanoscale upconverting materials, so-called upconverting nanoparticles (UCNPs), offer a wide range of potential applications for which the small size is a prerequisite.[4,5] Generally, these applications can be divided into two categories. For applications such as bio-imaging, sensing, and anti-counterfeiting, bright emission of upconverted light is key.[6–10] Conversely, applications such as photo-induced drug delivery, photodynamic and photothermal therapies, plant cultivation, and enhancing photovoltaics require not only bright emission but rely on high efficiency of the upconversion process as the emitted photons are used in subsequent photochemical or -thermal reactions.[11–18] For the latter, a high percentage of upconverted photons per absorbed low-energy photons, *i.e.*, high photoluminescence quantum yield, and a large amount of absorbed photons is highly desirable. While synthetic strategies have evolved over the past years, *e.g.*, dopant optimisation, host choice, core/shell architecture, in addition to computational approaches,[19–22] the relatively low quantum yield of UCNPs – maximum values of 13% have been reported to date[23] – remains one of the main challenges to bring these applications from proof of concept to real life. To advance computational models tackling these challenges, we here conduct an in-depth geometry optimisation study for different host matrices and their upconversion-inducing lanthanide dopants. It is expected that the reported results provide insights beneficial for the design of more efficient, next generation upconverting (nano)materials.

For the design of a meaningful geometry optimisation study, the accurate understanding of the upconversion process at an atomic level is helpful. The 4f–4f transitions of the trivalent lanthanide ions (Ln^{3+}) in centrosymmetric environments

[a]*Institute of Physical and Theoretical Chemistry, University of Tübingen, Tübingen (Baden-Württemberg), Germany. E-mail: Reinhold.fink@uni-tuebingen.de*
[b]*Department of Chemistry and Biomolecular Sciences, University of Ottawa, Ottawa, Ontario, Canada. E-mail: ehemmer@uottawa.ca*

† Electronic supplementary information (ESI) available. See DOI: https://doi.org/10.1039/d4nr04880f

are forbidden by Laporte's selection rule and therefore extremely weak. In non-centrosymmetric environments, this rule can be mitigated, and larger but still low transition rates are thus observed.[24,25] Moreover, the Ln^{3+} excited states have relatively long lifetimes, typically in the order of micro- or even milliseconds.[26] The transition probabilities of the lanthanides are therefore at a sweet spot that creates favourable conditions for an already excited Ln^{3+} ion to receive additional energy *via* photon absorption or energy transfer from neighbouring ions (before relaxation to the ground state can take place). The Ln^{3+} thereby reaches an even higher excited state and its radiative deexcitation to the ground state gives rise to upconverted photons.

Crystals of the type MXF_4 (M = alkali metal, X = lanthanides and yttrium) offer the required non-centrosymmetric doping sites and are therefore among the most commonly chosen host matrices for upconversion.[27–30] In addition, MXF_4 stands out due to the ease of substitution of a host ion (*e.g.*, Y^{3+}) by an emissive Ln^{3+} ion (*e.g.*, Er^{3+}, Tm^{3+}, or Yb^{3+}) given the comparable ionic radii as well as identical cation charge.[31] Furthermore, established synthetic access to nanomaterials of controlled size and (core/shell) architecture are available for these compounds.[29,32,33] Moreover, the prominence of specifically fluoride matrices is due to their comparatively high stability and the relatively low phonon energies reducing the probability for (non-radiative) quenching processes to take place.[34,35] Er^{3+} or Tm^{3+} are among the most widely studied dopants in these hosts, providing ladder-like energy levels for the upconversion process, while Yb^{3+} is commonly co-doped for its higher absorption cross section at 980 nm.[36–38]

Disordered host materials such as $NaYF_4$, which can crystallise in a cubic (α) or in a hexagonal (β) phase, have the added benefit of providing a variety of similar but not completely identical doping sites, which is advantageous for the upconversion process.[35,39,40] This study focuses on the observed structural disorder in the β-$NaYF_4$ crystal lattice, which is known to influence properties such as the exact energy level positions of dopants.[41] These on the other hand determine the energy difference to be overcome in energy transfer processes, as well as corresponding oscillator strengths and energy transfer rates.[35,40,42] The disorder of β-$NaYF_4$ and related compounds has long been established and discussed by experimentalists.[27,43–46] However, direct observation on an atomic level is difficult using methods such as X-ray diffraction alone, as this technique provides only averaged information over an ensemble of disordered sites in the crystal.[27,40,42,47]

Computational methods have been used in the past to explore the above-mentioned and other properties of β-$NaYF_4$, however, the employed models often lack consideration of lattice disorder.[48–52] If disorder has been considered, such as in the works by Platonenko *et al.* or Szefczyk *et al.*,[28,53] it was on the basis of discussing the possible unit cells of β-$NaYF_4$ and how disorder might combine the competing space group designations of β-$NaYF_4$. Huang *et al.* were the first ones to create a model of two supercells with different configurations but significantly altered the positions of Na^+ ions in the process by moving them to higher-symmetry lattice points.[54] Indeed, to the best of our knowledge, simulating more than two configurations of the created supercell for a given space group has so far not been reported for undoped β-$NaYF_4$. The knowledge gained from our study using several configurations of a large supercell has the potential to support the rational design of novel highly efficient upconverting materials, thereby aiding to solve the quest of increasing the upconversion yield and enlarging the scope of applications for these materials.

While our results confirm earlier assessments of the 1f Na^+–Y^{3+} disorder in β-$NaYF_4$ by Aebischer *et al.*,[27] more interestingly, our findings unveil the likely presence of additional configurations within the lattice at an atomistic level. Moreover, the influence of the 2h Na^+ disorder on the Ln^{3+} doping sites is reported for the first time on a purely *ab initio* computational level. Further insight is also given toward the slight disorder that is induced by low-percentage doping. The obtained results are validated by comparing the model to literature-reported experimental and theoretical data of $LiYF_4$, exhibiting a highly regular crystal structure, as well as published experimental data of disordered β-$NaYF_4$.

Structural setup

The process of determining the required size of the supercell for the calculation and the necessary number of configurations for each supercell is described in the following. Results obtained after optimising the individual structures are reported in Results and discussion.

Disordered β-$NaYF_4$

Lattice structure. In this work, the β-$NaYF_4$ structure is described in space group $P\bar{6}$, in which the Y-occuppied 1a sites are commonly placed at the edges of the lattice,[43] as reported in several other theoretical studies of this crystal.[28,48–50,52–54] This allows for a straightforward comparison of the obtained results to these studies. However, it should be noted that there also exist studies assigning space group $P6_3/m$ to β-$NaYF_4$.[51,55] In this case, Na^+ is placed at the edges of the lattice in the corresponding unit cell. A highly recommended, in-depth explanation and critical discussion of all possible space groups for β-$NaYF_4$ can be found in the review paper by Shi *et al.*[40] The unit cell of β-$NaYF_4$ in space group $P\bar{6}$ features three different cationic and two different anionic sites (Fig. 1A). The two anionic sites (Wyckoff positions 3j and 3k) are fully occupied by F^-, leaving no possibility for disorder. Among the cationic sites, one site exclusively accommodates Y^{3+} (Wyckoff position 1a). This site is nine-fold coordinated by three F^- at 3j sites and six F^- at 3k sites. These nine F^- form a tricapped trigonal prism with C_{3h} symmetry (Fig. 1B), in which the 3j F^- are located at the tips and the 3k F^- at the two caps of the prism. No disorder is possible at the 1a site. In contrast, finding Y^{3+} or Na^+ is equally likely (50% each) at the second cationic site (Wyckoff position 1f). Similar to the 1a site, this site is also coordinated by nine F^- with C_{3h} symmetry. The Wyckoff positions of the F^- that form the prism are swapped

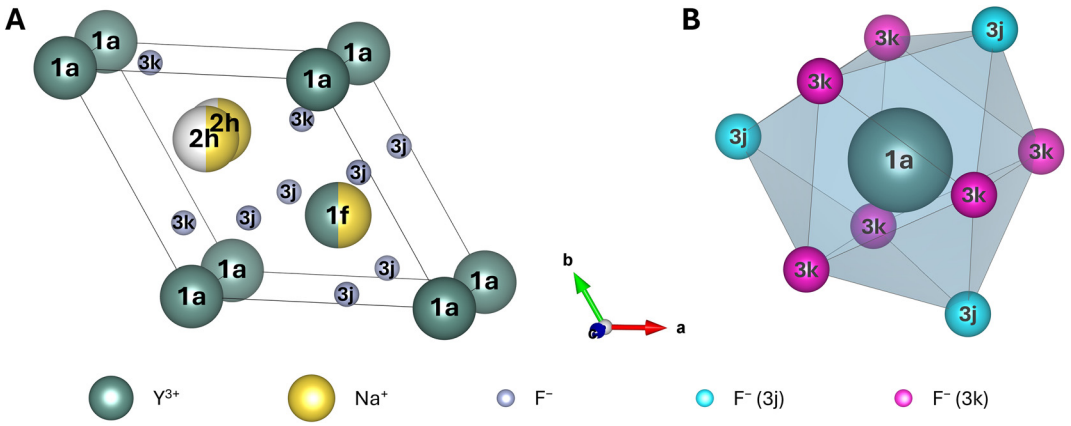

Fig. 1 (A) Unit cell of β-$NaYF_4$ with the composition $Na_{1.5}Y_{1.5}F_6$. Dark green spheres represent Y^{3+}, yellow spheres Na^+, white spheres are unoccupied sites, and small grey spheres represent F^-. Half spheres indicate a 50% occupation. (B) Both possible doping sites for Ln^{3+} (*i.e.*, 1a and 1f) are coordinated in a tricapped trigonal prismatic geometry by nine F^-. For clarity, the three 3j (caps) and the six 3k (trigonal prism) F^- are coloured in cyan and in pink, respectively. The prism for the 1f site is generated by rotating the coordination polyhedron shown in (B) by *ca.* 90° around the *c*-axis and swapping of the Wyckoff symbols for all F^-.

compared to the ones for the 1a site. When Ln^{3+} doping is considered, the Ln^{3+} ions randomly replace the Y^{3+} ions. Hence, the probability of finding an Ln^{3+} ion at a 1a site is twice as high ($^2/_3$) as the probability of finding the Ln^{3+} ion at a 1f site ($^1/_3$). Finally, the third cationic site is occupied by a single Na^+, split along the *c*-axis into two possible, equally likely sites (Wyckoff position 2h). In each unit cell only one of these two sites is occupied at a time. Both 2h positions are surrounded by six F^- with irregular octahedral symmetry.

The disorder at the 1f and the 2h site leads to more than one possible configuration for the unit cell, as will be explained further in the next subsection. Depending on the type of disorder (1f-, 2h-, or doping-originated), the positions of the F^-, forming the coordination polyhedral around the 1a and 1f sites, will be altered to a different extent. This in turn will reduce the symmetry elements available for the central site and therefore lower its point group. In most cases, even without doping, this changes the symmetry of most 1a and 1f sites from C_{3h} to C_1,[27] which significantly alters the properties of the potential Ln^{3+} dopants positioned at these 1a and 1f sites.

The available experimental evidence suggests that the occupation of the 1f site regularly alternates between Na^+ and Y^{3+} along all three spatial directions.[27] However, $NaYF_4$ and related materials are often synthesised at elevated temperatures, followed by thermal quenching, enabling energetically less favourable structural arrangements.[44,46] A regular alternation of Na^+ and Y^{3+} might therefore only be true as an averaged occupation over a large sample of unit cells. Indeed, if this regular alternation was the case, a larger unit cell with well-defined atomic positions at the 1f site could be generated. So far such a large unit cell has only been observed for β-$NaPrF_4$.[45,56] Local deviations at the 1f sites from the regularly alternating pattern on an atomic level and a less structured crystal with a higher degree of disorder therefore seem likely. Also, for the disorder at 2h sites only few theoretical studies have been conducted to date,[28,53,54] which leaves space for further investigation of the true atomistic structure of this disordered crystal.

To address these features of the β-$NaYF_4$ crystal, we developed a model that can represent disorder by creating several different configurations of the crystal structure. The required disorder was achieved by employing a large supercell, followed by alteration of the composition of the 1f and 2h sites within this supercell. Disorder at the 2h sites is straightforward to describe since the respective Na^+ occupies either one or the other Wyckoff 2h site within the unit cell. Moreover, supercells representing the disorder of the Wyckoff 1f sites also have to maintain the stochiometric composition of the crystal.

Supercell size. Depending on the inherent disorder of a unit cell, even small supercells that consist of only a few unit cells can result in an unmanageable large number of possible crystal structure configurations. For instance, any unit cell with one disordered site (like the Wyckoff 2h site), for which two possible ion occupations exist, has two possible configurations. The number of configurations in a supercell of such a crystal increases following a 2^N expression, where N is the number of unit cells in the supercell. For the 2 × 2 × 4 supercell chosen in this work, this leads to 2^{16} = 65 536 configurations formed by 16 individual unit cells for the 2h site. Additionally, for the 1f site of β-$NaYF_4$, we can distribute 8 Na^+ ions over 16 sites leading to $\binom{16}{8} = 12\,870$ configurations for this site, thus resulting in a total of more than 800 million configurations for both sites (*i.e.*, 1f and 2h). While symmetry considerations reduce these numbers, they stay much too large for computations. This is in stark contrast to $LiYF_4$, for which the completely ordered crystal is described by a single configuration, independent of the number of unit cells used.[57] Finding an appropriate supercell and a manageable

but sufficient number of configurations to describe the desired property is therefore a critical first step when creating a theoretical model for a disordered crystal.

To accurately describe the influence of the cation disorder, a 2 × 2 × 4 supercell has been chosen (Fig. 2). An in-depth discussion thereof is provided in the ESI.† In brief, a 2 × 2 × 4 supercell exhibits four rows of 1f sites along the *c*-axis. Three of these were altered when investigating disorder around the 1a site and one was altered for the investigation of the 1f site. Rows that were not neighbouring these sites are represented in faint colours in Fig. 2. These not neighbouring (faint) rows were occupied by an alternating sequence of Na^+ and Y^{3+}, which was kept fixed throughout all calculations. This simplification of the supercell induces some slight uncertainty with respect to the obtained results but the influence of these rows on the highlighted central sites should be marginal.

Occupational disorder, 1f site. For the following discussion it is assumed that the 2 × 2 × 4 supercell consisted of only six disordered 1f sites around the potential 1a and two disordered 1f sites around the potential 1f doping site (Fig. 2A and B, respectively). All other 1f sites are either coupled to one of these six/two sites, being of opposite type to prevent stoichiometric imbalances, or fixed to be either Na^+ or Y^{3+} (faint rows) and do not introduce further disorder into the 2 × 2 × 4 supercell. If the influence of the 1f disorder on (an Ln^{3+} located at) a 1a site is to be assessed (or more specifically on the F^- of the first anionic coordination sphere around the 1a site), the influence of all possible distributions of Na^+ and Y^{3+} at the six respective 1f sites of the first cationic coordination sphere is to be investigated. Stochastic considerations result in (2^6=) 64 different configurations (two possibilities for each of the six 1f sites). 13 of these 64 configurations are non-symmetry equivalent (neglecting the disorder at the 2h sites) and are to be calculated individually. A potential 1a doping site plus its first anionic and cationic coordination sphere (including six disordered 1f sites) is shown in Fig. 3A (corresponding to/extracted from configuration 10 of Table 1). The same cluster of ions is shown in Fig. 3C, this time with a different distribution of Na^+ and Y^{3+} at the 1f sites, belonging to configuration 5 of Table 1. Conversely, for the potential 1f doping site (2^2=) four different configurations can be generated, three of which are unique. Two of them are shown in Fig. 3B and D, corresponding to configuration 1 and 2, denoted in Table 1. The in total 16 different configurations (13 for the potential 1a and 3 for the potential 1f doping site) and the distributions of Na^+ and Y^{3+} onto the respective 1f sites for each of them are listed in Table 1. The same table also lists the ion at each of the six (two) 1f sites labelled in Fig. 3. We would like to emphasise at this point that the clusters of ions shown in Fig. 3 were created purely for better visualising the distribution of Na^+ and Y^{3+} at the 1f sites for the different configurations. These clusters are still embedded within their respective supercell. The remaining ions at the 1f sites in the supercell also change relative to the ions in the cluster, so that the stoichiometric ratio is retained. To recall, up to this point, no dopants have been introduced into the supercell. The close-up configurations shown in Fig. 3A and B correspond to the supercells shown in Fig. 2A (configuration 10) and Fig. 3B (configuration 1), respectively. As long as undoped, these configurations are identical and represent the configuration with the minimum energy after the optimisation process (*vide infra*).

Table 1 gives an overview of the various configurations created for the two clusters. By dividing the number of symmetry equivalent configurations (*i.e.*, degeneracy, second column) by the overall number of configurations for the individual cluster and multiplying by $^1/_3$ or $^2/_3$ for a potential 1f or 1a doping site, respectively, the weighting of this group of (symmetry equivalent) configurations is obtained (third column). The symmetry of the nine F^- around the central ion is also stated. These point groups are very crude approxi-

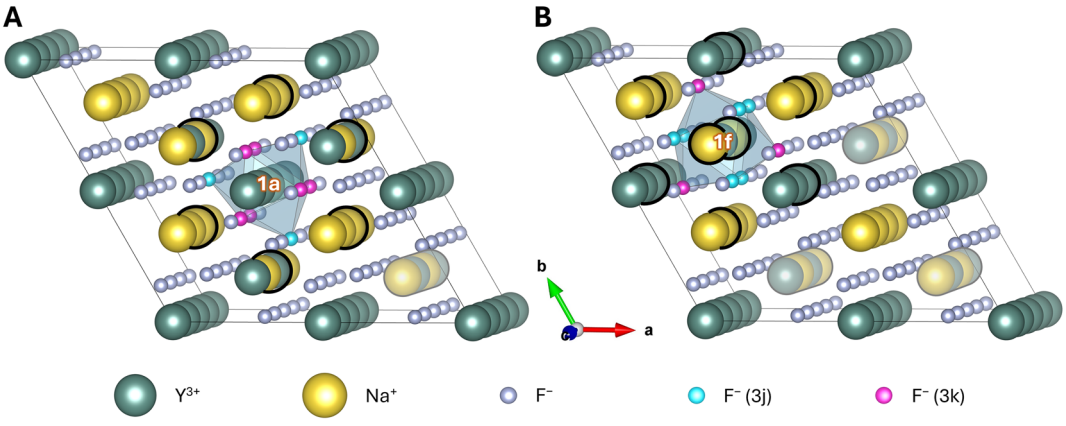

Fig. 2 2 × 2 × 4 supercell of β-$NaYF_4$ with the composition $Na_{24}Y_{24}F_{96}$. Highlighted are a potential (A) 1a and (B) 1f doping site (white labels), and their first anionic (F^- ions of the blue prism that are highlighted in cyan and pink) and cationic (Na^+ and Y^{3+} ions marked with a thick black circle) coordination spheres. Na^+ and Y^{3+} at the not neighbouring 1f rows (represented as faint) were not exchanged when creating the different configurations of the supercell. All other 1f sites were altered successively. For better visualisation, a close-up of the two potential doping sites with their nearest ions is shown in Fig. 3A and B.

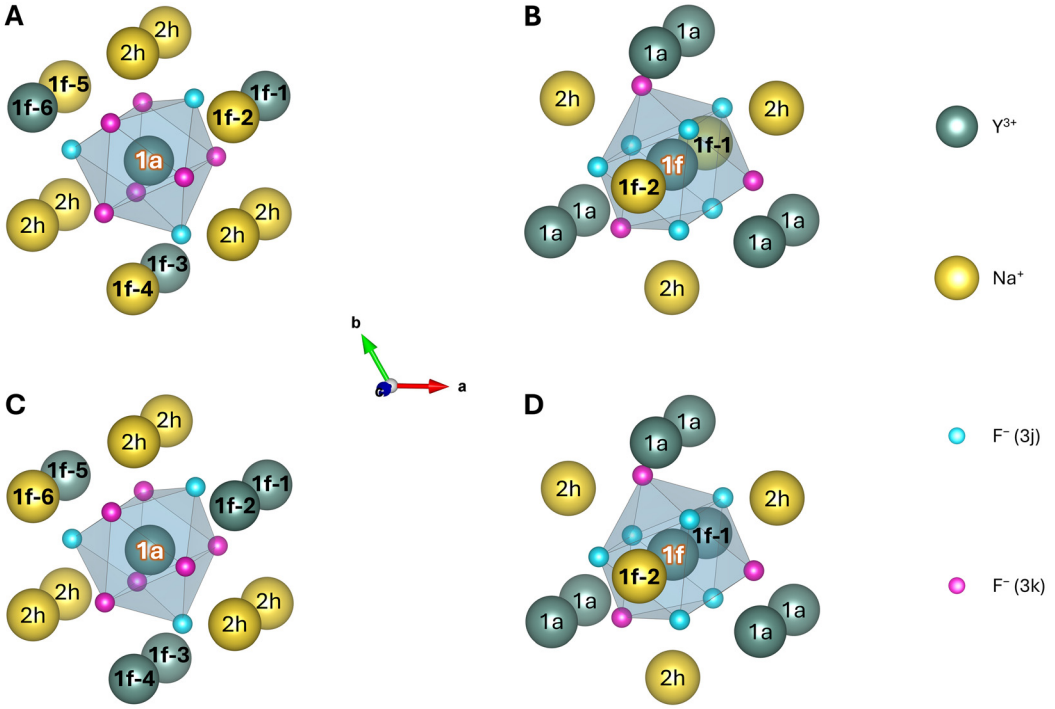

Fig. 3 Potential (A) 1a and (B) 1f doping sites and their first anionic and cationic coordination spheres for the supercells shown in Fig. 2A and B, respectively. The corresponding supercells are designated as configuration (A) 10 and (B) 1 in Table 1. Two additional configurations are shown in C and D, corresponding to configuration 15 and 2, respectively, in Table 1. Here some of the 1f sites were altered in comparison to configuration 10 and 1. For all clusters the 1a, 1f, and 2h sites are labelled by their Wyckoff symbols, the central site is labelled in white. The 1f sites for which the distribution of Na^+ and Y^{3+} were altered in this study are set in bold and numbered from (1f-) 1 to 6 (panels A and C) and 1 to 2 (panels B and D) for the potential 1a and 1f doping sites, respectively. The numbering of these sites is equivalent to the scheme used in the last column of Table 1. All clusters presented here were created for visualisation purposes only and are still embedded in their respective supercells used for the geometry optimisation.

Table 1 List of generated configurations for the potential 1f (1 to 3) and 1a (4 to 16) doping sites, their degeneracy, weighting, idealised F^- symmetry, and Na^+/Y^{3+} distribution at the 1f sites as shown in Fig. 3

Configuration	Degeneracy	Weighting (%)	F^- symmetry	Na^+/Y^{3+} distribution at neighbouring 1f sites					
Site: 1f	**4**	**33.3**		**1**	**2**				
1	1	8.3	C_{3h}	Na^+	Na^+				
2	2	16.7	C_3	Y^{3+}	Na^+				
3	1	8.3	C_{3h}	Y^{3+}	Y^{3+}				
Site: 1a	**64**	**66.7**		**1**	**2**	**3**	**4**	**5**	**6**
4	1	1.0	C_{3h}	Na^+	Na^+	Na^+	Na^+	Na^+	Na^+
5	6	6.3	C_1	Na^+	Na^+	Na^+	Na^+	Na^+	Y^{3+}
6	3	3.1	C_{3h}	Na^+	Na^+	Na^+	Na^+	Y^{3+}	Y^{3+}
7	6	6.3	C_1	Na^+	Na^+	Na^+	Y^{3+}	Y^{3+}	Na^+
8	6	6.3	C_1	Na^+	Na^+	Y^{3+}	Na^+	Y^{3+}	Na^+
9	2	2.1	C_3	Y^{3+}	Na^+	Y^{3+}	Na^+	Y^{3+}	Na^+
10	6	6.3	C_1	Y^{3+}	Na^+	Y^{3+}	Na^+	Na^+	Y^{3+}
11	12	12.5	C_1	Y^{3+}	Y^{3+}	Na^+	Y^{3+}	Na^+	Na^+
12	6	6.3	C_1	Y^{3+}	Y^{3+}	Y^{3+}	Na^+	Y^{3+}	Na^+
13	6	6.3	C_1	Y^{3+}	Y^{3+}	Na^+	Y^{3+}	Y^{3+}	Na^+
14	3	3.1	C_{3h}	Y^{3+}	Y^{3+}	Y^{3+}	Y^{3+}	Na^+	Na^+
15	6	6.1	C_1	Y^{3+}	Y^{3+}	Y^{3+}	Y^{3+}	Y^{3+}	Na^+
16	1	1.0	C_{3h}	Y^{3+}	Y^{3+}	Y^{3+}	Y^{3+}	Y^{3+}	Y^{3+}

mations that only consider shifts of the F^- along the *c*-axis, depending on the nearest neighbouring ions at the 1f sites as suggested by Aebischer *et al.*[27] Because of the differing ionic radii, Na^+ pushes the closest F^- stronger away than Y^{3+} (along the *c*-axis). This approximation is less valid when incorporating shifts along the other two axes and breaks down comple-

tely when considering changes introduced by Na^+ at the disordered 2h sites.[40] However, it is a helpful designation to understand the influence of the different distributions of Na^+ and Y^{3+} at neighbouring 1f sites onto the F^-. The last column of Table 1 states the distribution of Na^+ and Y^{3+} onto the six (two) 1f sites shown in Fig. 3.

To give an example, for configuration 5, five additional symmetry equivalent configurations exist. This can easily be deduced from the five Na^+ and one Y^{3+} that are distributed among the six 1f positions around a 1a site. The single Y^{3+} can be placed at each of the six positions, and the five remaining Na^+ are all equivalent (their placing order therefore does not matter). The total number of configurations for a 1a site is 64. Therefore, an Ln^{3+} ion doped into β-$NaYF_4$ has a probability of $6/64 \cdot {}^2/_3 = 0.0625$ or 6.3% to be located in an environment of this or an equivalent configuration. All of these considerations are purely with respect to geometric aspects. The energetic difference between individual configurations determines their actual occurrence in a real crystal and will be examined after the geometry optimisation. Finally, the positions of the F^- were considered to determine the point group of the central ion. The 1f sites 5 and 6, consisting of one Na^+ and one Y^{3+}, influence one of the F^- by moving it closer to Y^{3+}, while all other F^- stay in place. This reduces the point group around the central 1a site from C_{3h} to C_1.

The configurations listed in Table 1 were generated and energetically optimised as described in the computational details.

Occupational disorder, 2h site. So far, only the influence of the 1f sites onto the F^- has been considered. As stated above, the cations at the 2h sites, fully occupied by Na^+, also possess disorder (along the *c*-axis). However, including their influence on the positions of the F^- in the same manner as done for the 1f site was not feasible. The number of possible configurations would significantly increase as stated in the introduction. Computing such a large number of configurations constitutes a significant computational challenge.[48–51] Therefore, the 2h disorder was commonly neglected.

Nonetheless, to estimate the potential impact of the 2h disorder, three representative 2h configurations were selected and calculated. Therefore, one possible distribution was chosen for the in total 16 Na^+ at 2h sites in a 2 × 2 × 4 supercell (referred to as Na1) and used for all subsequent calculations. The occupied sites were chosen so that an equal amount of Na^+ was displaced along the +c- and −c-axis in each unit cell, reflecting the average distribution in a real crystal. After energetically minimising all configurations for the different Na^+/Y^{3+} distributions at the 1f sites, the 2h distribution was adjusted for the energetically most stable structure (configuration 10). This resulted in the creation of configurations 10-Na1, -Na2, and -Na3. Na1 is the distribution of Na^+ at the 2h site used initially (and for all other configurations of β$NaYF_4$). Na2 is another *c*-axis balanced distribution (see above). However, in comparison to Na1, in Na2 the Na^+ were shifted differently along the *c*-axis. Finally, for Na3 the eight Na^+ closest to the potential doping site were all displaced along the −*c*-axis. After creating these two additional configurations (*i.e.*, Na2 and Na3), the structures were optimised a second time. Optimization of these two configurations, Na2 and Na3, and their comparison to configuration Na1 provided evidence that the influence of the 2h disorder on the potential doping sites is less significant than the disorder at the 1f sites (*vide infra*). Therefore, no additional 2h disordered configurations were created.

Ln^{3+}-doping (Ln = Er, Tm, and Yb). To account for Ln^{3+}-doping, 48 doped configurations were created in addition to the 16 undoped configurations shown in Table 1. For this purpose, each of the optimised configurations was doped consecutively with Er^{3+}, Tm^{3+}, and Yb^{3+} at the central 1a or 1f site as highlighted in Fig. 3. Furthermore, the two additional 2h configurations were doped with Er^{3+} at the central 1a site. Subsequently, all doped structures were optimised to an energetic minimum structure. For one configuration (number 10 in Table 1) doped with Er^{3+}, the optimisation process was repeated with a larger basis set for Er^{3+} (TZV2P instead of DZVP) to estimate the influence of the latter (*vide infra*).

Overall, the 2 × 2 × 4 supercell consists of 144 ions, 24 of which being Y^{3+}. Replacing one of these Y^{3+} ions by an Ln^{3+} results in a doping concentration of 4.2 mol%. Doping concentrations, especially for activator ions such as Er^{3+} and Tm^{3+}, are usually well below these values. In fact, the most common doping concentrations for Er^{3+} and Tm^{3+} are 2 mol% and 0.5 mol%, respectively.[58,59] However, enlarging the supercell further (and thereby reducing the doping concentration) is limited by the steeply increasing computational demand and was therefore not carried out.

Ordered $LiYF_4$

Extension of the model. To demonstrate the validity of our computational protocol, $LiYF_4$ (Fig. 4) as a popular alternative host lattice for upconverting (nano)materials was modelled with the same method. Unlike β-$NaYF_4$, $LiYF_4$ crystallizes in a tetragonal crystal structure (space group $I4_1/a$) in which all lattice sites are fully occupied by a single type of ion.[57] Consequently, $LiYF_4$ constitutes an easier case than β-$NaYF_4$ with only one position for Li^+ (Wyckoff symbol 4a), one for Y^{3+} (Wyckoff symbol 4b), and one for F^- (Wykoff symbol 16f). The unit cell of $LiYF_4$ and the coordination polyhedron around the Y^{3+} sites, *i.e.*, a distorted square antiprism, are shown in Fig. 4A and B, respectively. Based on this unit cell, a 3 × 3 × 1 supercell with 216 ions was created (Fig. S2†). For this supercell, a doping rate of 2.8% is obtained upon replacement of 1 of the 36 Y^{3+} by an Ln^{3+}. Following the optimization of the undoped $LiYF_4$ structure, one of the 4b sites was doped consecutively with Er^{3+}, Tm^{3+}, and Yb^{3+}, and the three resulting structures were optimised once again.

Computational details

DFT with CP2K. All calculations were performed by applying periodic density functional theory (DFT) as implemented in

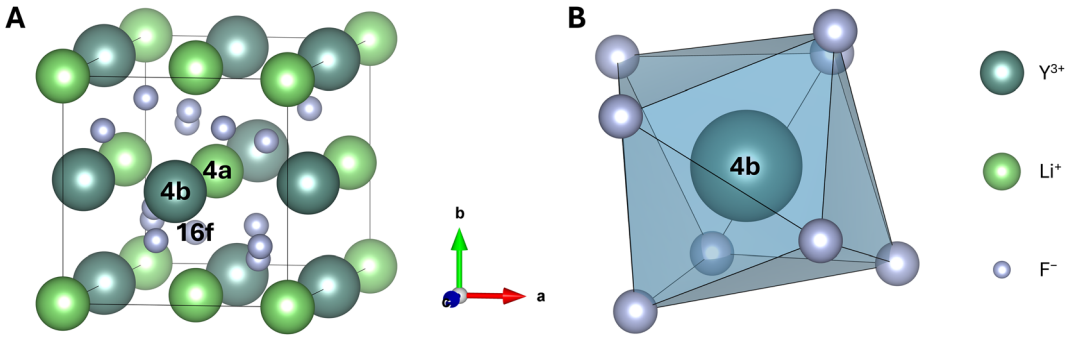

Fig. 4 (A) Unit cell of $LiYF_4$ with the composition $Li_4Y_4F_{16}$. Dark green spheres represent Y^{3+}, light green spheres Li^+, and small grey spheres represent F^-. $LiYF_4$ features only one potential doping site, *i.e.*, Wyckoff position 4b. (B) Coordination polyhedron around Y^{3+}. Each Y^{3+} at a 4b site is surrounded by eight F^- ions, creating a distorted square antiprism.

the software package CP2K, version 7.1.[60] CP2K utilises atomic Gaussian type orbitals (GTOs) in its calculations.[61–63] For Li^+, Na^+, F^-, and Y^{3+}, basis sets of split valence triple-zeta quality with double polarisation functions (TZV2P-MOLOPT-SR) were employed consistently during all calculations. The lanthanides (Er^{3+}, Tm^{3+}, and Yb^{3+}) were modelled using basis sets of double-zeta quality (DZVP-MOLOPT-SR), except for an additional study on Er^{3+} where TZV2P-MOLOPT-SR was used as well.[64] The electron-core interaction was described by using Goedecker, Teter, and Hutter (GTH) type norm-conserving pseudopotentials,[65] while exchange and correlation were expressed *via* the Perdew–Burke–Ernzerhof (PBE)[66] exchange–correlation functional. To account for dispersion, the Grimme D3 correction was applied.[67] The electron densities were expanded in plane waves, with the cutoff and relative cutoff energy corresponding to 800 Ry and 60 Ry, respectively. A 2 × 2 × 2 and a 2 × 2 × 3 Monkhorst–Pack k-point mesh was utilised to sample the reciprocal space for the β-$NaYF_4$ and $LiYF_4$ supercells, consisting of 144 and 216 atoms, respectively. The convergence criterion for the self-consistent field cycle was set to 10^{-6}. Input files for the calculation of the two different crystals are provided in the ESI.† All figures were drawn with the VESTA software package.[68]

Table 2 Comparison of (A) lattice parameters, (B) bond distances, and (C) band gaps of $LiYF_4$ obtained in this study with experimental and theoretical data taken from the available literature

$LiYF_4$	Lattice parameters (Å)			
A	$a = b$	c	Deviation (%)	Ref.
Experimental	5.26	10.94	—	57
Theoretical	5.13	10.67	2.5	70
Theoretical	5.17	10.82	1.5	71
Theoretical	5.20	10.80	1.2	This work
	Bond distances (Å)			
B	Y^{3+}–$F^-_{(1)}$	Y^{3+}–$F^-_{(2)}$	Deviation (%)	Ref.
Experimental	2.407	2.453	—	57
Theoretical	2.244	2.304	6.4	73
Theoretical	2.265	2.309	5.9	This work
C	Band gap (eV)		Deviation (%)	Ref.
Experimental	> 10.77		—	71 and 76
Theoretical	8		25.7	74
Theoretical	11.09		3.0	71
Theoretical	8.08		25.0	This work

Results and discussion

Undoped and doped (Er^{3+}, Tm^{3+}, Yb^{3+}) minimum energy structures for different configurations of β-$NaYF_4$ in a 2 × 2 × 4 supercell were calculated with the settings described above. The same was done for the single available configuration of $LiYF_4$ in a 3 × 3 × 1 supercell. The structures were evaluated in terms of relative energies, lattice parameters, and Y^{3+}–F^- bond lengths. These properties were then compared to experimental and theoretical data, if available.

Validation of the model

Ordered $LiYF_4$. $LiYF_4$ exhibits only one configuration, which renders the comparison of the obtained results with other data sets from the literature straightforward (Table 2). Therefore, $LiYF_4$ was chosen for a first evaluation of the model, prior to application of the computational setup to more complex lattices, such as β-$NaYF_4$. Deviations in this study were consistently calculated as the absolute value of the difference between the experimental value from literature and the (here) calculated theoretical values, divided by the experimental value. Also, the deviations listed in this text were calculated explicitly and not taken from the literature. The calculated lattice parameters for $LiYF_4$ deviated slightly by 1.2% from the experimental values reported by Thoma *et al.*[57] An even smaller deviation of 0.4% was obtained in comparison to work by Keller *et al.*, but little detail about crystal synthesis and characterisation was provided by the authors.[69] The values calculated in our study also compared nicely to other computational works by Ching *et al.* and Luong *et al.*, reporting unit cells, which deviated by 1.5 to 2.5% from the experimental data referenced above.[70,71]

It should be mentioned that the authors of both abovementioned computational studies stated a smaller discrepancy to experimental values. However, both referenced a $LiYF_4$ crystal structure by Garcia *et al.* that was synthesised adding 2 wt% of PrF_3.[72] Even though the influence of the dopant on the lattice structure is small (*vide infra*), comparison to an undoped sample is still preferable. For pure $LiYF_4$ and the 2 wt% of Pr^{3+} containing crystals average bond lengths for two types of Y^{3+}–F^- bonds were obtained.[57,72] Determination of the Y^{3+}–F^- bond lengths for the crystal structure optimised in our study unveiled discrepancies to the experimental values of 5.8% and 0.7%, respectively. Yin *et al.* calculated the same bond lengths for pure $LiYF_4$, and deviations were at a similar range (6.4% and 0.2%, respectively).[73] With respect to the calculated band gap, our results very closely matched computed values that used a functional of the same type (generalized gradient approximation, GGA).[74,75] However, both our and their computational studies deviated from the experimental value by about 25%.[71,76] In fact, calculations describing exchange and correlation by GGA type functionals are known to underestimate the band gap of semiconductors and insulators.[77] Hence, our calculated values were within the expected margin of error. Better results can be achieved with more sophisticated methods, if required.[71] Our results further demonstrated that doping the structure with Er^{3+}, Tm^{3+}, or Yb^{3+} only marginally changes the lattice structure (on average less than 1% for all three dopants). This is most likely due to the small doping concentration and the similarity of the ionic radii. This will be discussed in more detail for β-$NaYF_4$. Thus, all values assessed suggest that our approach is well suited for predicting structural parameters of inorganic crystals beyond $LiYF_4$.

Disordered β-$NaYF_4$. In the case of β-$NaYF_4$, the predicted values for the 16 individual configurations were averaged with respect to their weighting (Table 1). Table 3 provides a summary of the obtained data, including data taken from the literature. Compared to macroscopic crystals synthesised and characterised by Roy *et al.*, slightly larger lattice parameters *a* and *b* and a slightly smaller parameter *c* were predicted by the designed model.[45] As the disorder affects the symmetry of the crystal, *a* and *b* were found to be no longer equal in length. However, it should be noted that the difference between these values was less than 0.01%, and the angle γ was only 0.1% larger than the experimental value of 120°. Overall, the size of the unit cell changed by only 0.9%. These findings are in very good agreement with other theoretical calculations, such as the ones by Platonenko *et al.* or Park *et al.*, who predicted very similar values.[28,52] Moreover, the bond length between Y^{3+} and F^- averaged over all nine bonds yielded a 1.2% shorter bond length compared to experimental results,[45] being in good agreement with the literature. For instance, a different computational model by Yao *et al.* predicted a 5.9% shorter bond length.[49] With respect to band gap calculations, as seen for $LiYF_4$, the calculated band gap was also underestimated for β-$NaYF_4$, namely by 8.9% compared to the experimental value.[78] Again, this value is in line with previously reported computational results (10.4%) that used the same type of functional.[48] Similar to $LiYF_4$, doping the structure with Er^{3+}, Tm^{3+}, and Yb^{3+} generated only minor overall changes, as detailed in the following section (Impact of disorder for β-$NaYF_4$).

Table 3 Comparison of (A) lattice parameters, (B) bond distances, and (C) band gaps of β-$NaYF_4$ obtained in this study with experimental and theoretical data taken from the available literature

β-$NaYF_4$	Lattice parameters (Å)			
A	$a = b$	c	Deviation (%)	Ref.
Experimental	6.00	3.58	—	45
Theoretical	6.07	3.53	1.3	52
Theoretical	6.01	3.60	0.3	28
Theoretical	$6.04 \neq b$	3.54	0.9	This work
	Bond distance (Å)			
B	Y^{3+}–F^-		Deviation (%)	Ref.
Experimental	2.371		—	45
Theoretical	2.230		5.9	49
Theoretical	2.342		1.2	This work
C	Band gap (eV)		Deviation (%)	Ref.
Experimental	= 8		—	78
Theoretical	= 7.17		10.4	48
Theoretical	= 7.83		2.1	52
Theoretical	= 7.29		8.9	This work

Thus, we have demonstrated the suitability of our protocol to predict lattice parameters and average bond lengths for two lattices with different crystallographic properties, *i.e.*, $LiYF_4$ and β-$NaYF_4$, with reasonable accuracy. The chosen approach of averaging over 16 different configurations for β-$NaYF_4$ indeed provided results that are close to reported experimental values. More importantly though, now that individual configurations have been created and optimised, they can be compared to each other, and possible trends may be deduced.

Impact of disorder for β-$NaYF_4$

Occupational disorder, 1f site. Aebischer *et al.* considered the cation disorder for β-$NaLaF_4$ and related compounds such as β-$NaYF_4$.[27] Based on patterns obtained *via* diffuse X-ray scattering and Monto Carlo simulations, they concluded that the 1f site preferentially produces rows of regularly alternating Na^+ and La^{3+} along the *c*-axis. Furthermore, it was theorised that the positions of Na^+ and La^{3+} within these rows are interchanged for two neighbouring 1f rows. For each 1f row, six such neighbouring rows exist (a set of four neighbouring 1f rows is shown in Fig. 4). The results of our computational model further validate this claim; the configuration that consists of alternating rows resulted in the lowest lattice energy (*i.e.*, configuration 10). For reference, ΔE in Table 4 and Table S1† represents the difference between the energy of the respective configuration and the overall energetically lowest configuration (of the respective undoped or doped structure). It becomes clear that configuration 10 (and 1, which is identi-

Table 4 Results of the structural optimisations for the 16 different configurations of undoped β-$NaYF_4$. Lattice energies relative to the most stable configuration (ΔE), deviations of the lattice parameters from the experimental values ($Dev._{LP}$), and averaged bond lengths (Y^{3+}–F^-) are displayed. For β-$NaYF_4$ doped with 4.2% Er^{3+} only the energy differences are showcased (additional data for β-$NaYF_4$ doped with Er^{3+}, Tm^{3+}, and Yb^{3+} are provided in Table S1†)

		Undoped β-$NaYF_4$			4.2% Er^{3+}
Site	Config.	ΔE (kJ mol^{-1})	$Dev._{LP}$ (%)	Y^{3+}–F^- (Å)	ΔE (kJ mol^{-1})
1f	1	0.0	0.77	2.347	0.1
	2	1.9	0.83	2.342	2.4
	3	3.4	0.90	2.338	3.4
1a	4	6.5	0.78	2.372	6.5
	5	4.6	0.85	2.354	4.6
	6	4.3	0.88	2.360	3.4
	7	1.9	0.88	2.346	1.8
	8	1.8	0.92	2.345	1.8
	9	1.2	0.86	2.336	1.2
	10	0.0	0.77	2.338	0.0
	11	2.6	0.87	2.344	1.6
	12	1.9	0.92	2.333	1.9
	13	2.0	0.86	2.335	2.3
	14	4.8	0.89	2.336	4.8
	15	4.2	0.84	2.330	4.2
	16	7.9	0.76	2.326	8.3

cal to 10 as long as being undoped, Fig. 3) has the lowest lattice energy of all assessed configurations (ΔE = 0 as it exhibits the minimum energy). All other configurations are higher in energy. It is also noteworthy that the energies of all examined configurations follow the pattern of lower energy for regularly alternating distributions (configurations 7 to 13) to higher energies for configurations with more locally clustered Na^+ and Y^{3+} (configurations 4 to 6 and 14 to 16, respectively).

Another important parameter to assess is the deviation of the lattice parameters (Dev_{LP}, Table 4). This parameter describes the deviation of the calculated lattice parameters from the experimental values and was obtained by averaging over the relative deviations of the individual cell vectors. Again, configuration 10 featured one of the smallest deviations. The highly regular alternation of Na^+ and Y^{3+} for this configuration is probably the main reason for the low lattice energy and small lattice parameter deviation observed. However, the difference in lattice energy for the remaining 14 configurations is at most 7.9 kJ mol^{-1}, even for the two configurations with the most locally clustered distributions of Na^+ and Y^{3+} (configuration 4 and 16 with six Na^+ and six Y^{3+}, respectively).

Indeed, nanoparticles of this crystal type are typically synthesised at temperatures of up to 300 °C. At this temperature, the Boltzmann population of the energetically most unfavourable configuration (configuration 16) amounts to 0.19 (Table 5) as compared to the most stable configuration (configuration 10). Under the assumption of elevated synthesis temperatures and rapidly cooled crystallites, all configurations are therefore likely to be present (locally) in such a crystal. Adding to this, the sample used for characterisation by Aebischer *et al.* was

Table 5 Occupation probability and percentage of C_1 symmetry according to Boltzmann distribution for a potential 1a doping site (configurations 4 to 16). In the first part of the table (all columns except the last one) the occupation probability, $f(E_n)/f(E_{10})$, for each configuration relative to the energetically lowest configuration (*i.e.*, configuration 10) is calculated at three different temperatures (*i.e.*, 20, 300, and 590 °C), where k_B is the Boltzmann and N_A the Avogadro constant. The weighting of each configuration according to the statistical distribution as presented in Table 1 is given in the bottom row of the table. In the last column of this table, the percentage of configurations with C_1 symmetry relative to all configurations is calculated, taking into account the Boltzmann distribution at the three different temperatures (*i.e.*, T = 20, 300, and 590 °C) and only the statistical weighting ($T = \infty$; from top to bottom)

n (=configuration) symmetry		4 C_{3h}	5 C_1	6 C_{3h}	7 C_1	8 C_1	9 C_{3v}	10 C_1	11 C_1	12 C_1	13 C_1	14 C_{3h}	15 C_1	16 C_{3h}	Total C_1 (%)
$\Delta E = E_n - E_{10}$ (kJ mol^{-1})		6.509	4.588	4.331	1.901	1.791	1.180	0	2.586	1.911	2.002	4.801	4.158	7.948	
$\frac{f(E_n)}{f(E_{10})} = e^{-\frac{\Delta E}{k_B \cdot N_A \cdot T}}$	T = 20 °C	0.07	0.15	0.17	0.46	0.48	0.62	1.00	0.35	0.46	0.44	0.14	0.18	0.04	91.1
	T = 300 °C	0.26	0.38	0.40	0.67	0.69	0.78	1.00	0.58	0.67	0.66	0.37	0.42	0.19	88.7
	T = 590 °C	0.40	0.53	0.55	0.77	0.78	0.85	1.00	0.70	0.77	0.76	0.51	0.56	0.33	87.5
Weighting (%)		1.0	6.3	3.1	6.3	6.3	2.1	6.3	12.5	6.3	6.3	3.1	6.3	1.0	84.4

prepared at even higher temperatures, *i.e.*, 590 °C.[27,46] At such high temperature, the expected relative population of configuration 16 is as high as 0.33. On the other hand, once a reaction mixture has cooled down, especially if quenched, a positional change of Na^+ and Y^{3+} to produce energetically favourable alternating rows after the formation of a disordered crystal is unlikely as ion swapping is associated with a significant energy barrier.[44,46,79] Considering Boltzmann distribution and the statistical weighting (Table 5), it can also be deduced that for temperatures above 170 °C configuration 11 is the most likely to be found in a crystal. This is because the statistical weighting of configuration 11 is twice as high as that of configuration 10, and its occupation probability raises above 0.5 at this temperature compared to configuration 10. Furthermore, it must be emphasized that, in principle, configurational entropy has to be considered for the disordered configurations as well, thus, making their occurrence even more likely.

The original report by Aebischer *et al.* also mentions symmetry considerations supporting that configuration 10 might be the most likely one.[27] Nonetheless, this configuration is definitely not the only one to be found in such a crystal. The authors conducted Monte Carlo simulations from which they deduced that in 93–95% of the modelled cells the surrounding of a 1a site was reduced to C_1 symmetry because of the disorder at the 1f site and its influence on the F^- surrounding the 1a site. However, if all 1f rows strictly followed the previously proposed alternation along the *c*-axis, every single 1a site must be of C_1 symmetry (=100%). This is because each 1a cluster will have two 1f rows with opposite Na^+/Y^{3+} allocation in their first cationic coordination sphere. Each of them will therefore push one F^- of the 1a site into different (opposite) directions, resulting in C_1 symmetry.

The discrepancy between 93–95% and 100% C_1 symmetry can be partially explained through the data made available by this study. When looking at the distribution of the different symmetries through the weighted average of the configurations for a potential 1a doping site (Table 1, configuration 4 to 16), 84.4% of these configurations will be of C_1 symmetry (*i.e.*, 54 of the in total 64 configurations; last column of Table 5). If furthermore varying occupational probabilities between these different configurations (induced by their relative energetic differences) *via* Boltzmann distribution are considered, almost 89% of the potential doping sites (depending on the temperature) should be of C_1 symmetry. While this does not provide direct evidence for the actual symmetry distribution around the 1a sites, it strongly suggests that there is deviation from the energetically favoured strictly alternating 1f rows.

Also, it should be noted that all symmetry considerations are invalidated once the disorder at the 2h sites is considered. Except for specific and rather rare configurations of the six 2h Na^+ around a 1a site, these Na^+ remove any remaining symmetry elements by pushing the closest F^- in different directions, resulting in C_1 symmetry for most if not all 1a (and also 1f) sites. Based on all of the above aspects of symmetry and energetic consideration, we therefore concluded that the F^- around the 1a sites were considerably more disordered than suggested by Aebischer *et al.*, and that probably almost all 1a and 1f sites were of C_1 symmetry.

Aebischer *et al.* additionally mentioned a displacement of the three 3j F^- along the *c*-axis in between two neighbouring 1f sites depending on the distribution of Na^+ and La^{3+} at these sites.[27] It was stated that an F^- between a pair of Na^+ and La^{3+} at adjacent 1f sites will be displaced by 0.07 Å towards La^{3+} because of the larger ionic radius of Na^+. Thereby, the bond between F^- and La^{3+} is shortened as evidenced in the datasets generated in our study. In configuration 1, the central 1f Y^{3+} has two Na^+ at the two neighbouring 1f sites (Fig. 2B, and Table 1). Such an arrangement is quite different from configuration 3, in which the two neighbouring 1f sites are both occupied by Y^{3+}. While the average bond length for all nine F^- presented in Table 4 suggests that configuration 3 has shorter bonds (contrary to the Monte Carlo model of Aebischer *et al.*),[27] a detailed analysis revealed that the bonds between Y^{3+} and the six 3j F^- in configuration 1 were indeed shortened on average by 0.03 Å compared to configuration 3 (one bond is even reduced by 0.08 Å). The apparent elongation in the averaged result can be explained by the three 3k F^- that show a significant increase in bond length by 0.04, 0.09, and 0.14 Å. The discrepancies (*i.e.*, shorting by 0.03 Å compared to 0.07 Å) between these *ab initio* results and the Monto Carlo model can either be rooted in the model itself, the different ions being used (although the ionic radius of Y^{3+} is smaller than that of La^{3+}, and therefore, a larger and not smaller displacement of the six 3j F^- for Y^{3+} seems therefore plausible), or possibly in the different occupation of Na^+ at the 2h sites. While Aebischer *et al.*[27] did not report on the 2h sites, our results provide evidence that these sites have significant influence on the bond lengths (see next section).

Similar to the potential 1f doping site, the general trend observed for the Y^{3+}–F^- bond lengths at the 1a sites can be summarised as following: the more of the neighbouring 1f sites were occupied by Na^+, the more distorted prisms as well as overall longer average bond lengths (Table 4) were observed. In summary, the distribution of Na^+ and Y^{3+} at the 1f sites has a significant influence on the position of both the 3j and 3k F^- and thereby has a profound impact on the coordination sphere of Ln^{3+} ions at both the 1a and 1f sites.

Occupational disorder, 2h site. Encompassing all structural variations that were generated by the Na^+ configurations at the disordered 2h sites in a 2 × 2 × 4 supercell is neither practical nor particularly informative. Instead, 3 different 2h-disordered structures of configuration 10 were created and optimised to gain a first insight into this type of disorder. The results of this approach are presented in Table 6A. Note that by introducing the 2h disorder, the six-fold degeneracy of configuration 10 (as shown in the second column of Table 1) is lifted, increasing the number of 2h disordered configurations from 6 to 384 (64 × 6; though, some of these are symmetry equivalent). To limit the computational demand and since preliminary results indicated that the 2h disorder had less influence on the crystal structure than the 1f disorder, only these three configurations were investigated.

Table 6 Comparison of lattice energies relative to configuration 10 (ΔE), deviations of the lattice parameters ($Dev._{LP}$), and bond lengths (Y^{3+}–F^-) for different Na^+ distributions (NaX) at the 2h sites of configuration 10 for undoped (A) and Er^{3+}-doped (B) β-$NaYF_4$

NaX	ΔE (kJ mol^{-1})	$Dev._{LP}$ (%)	Y^3–F^- (Å)
A	**β-$NaYF_4$**		
Na1	0.0	0.77	2.338
Na2	0.1	0.79	2.334
Na3	1.4	0.81	2.332
B	**β-$NaYF_4$: 4.2% Er^{3+}**		
Na1	0.0	0.76	2.338
Na2	0.8	0.82	2.334
Na3	1.7	0.93	2.330

Changing the disorder at the 2h sites randomly but c-axis balanced (Na1 to Na2) resulted in rather insignificant changes in the lattice energy of 0.1 kJ mol^{-1}. Even aligning all Na^+ closest to the central ion towards one direction (Na3) increased the lattice energy by only 1.4 kJ mol^{-1}. These values are smaller than most energy difference observed when changing the occupation of Na^+ and Y^{3+} at the 1f-disordered sites (third column of Table 3). Deviations of the lattice parameters and average bond lengths were more pronounced, although still small when considering the significant changes observed from the 1f disorder. A noteworthy change induced by the 2h disorder is the observed reduction of individual Y^{3+}–F^- bond lengths of up to 0.05 Å when a 2h Na^+ is very close to or aligning with the central 1f site along the *c*-axis (compared to a structure where it is placed much further away). The corresponding 3k F^- in between the 2h Na^+ and the 1f site is thereby pushed closer to the 1f site by the 2h Na^+. Overall, the influence of the Na^+ at the 2h sites onto the F^- very much resembles that of Na^+ and Y^{3+} at the 1f sites. In both cases, the closest F^- is pushed away from its ideal position. Therefore, disorder at 2h sites might not have as much of an impact on the overall crystal structure but great local influence on the positions of specific F^-. With small energetic differences between individual distributions of Na^+ at 2h sites, a high prevalence of different arrangements can be expected. At the same time, the presumably significantly lower energy barrier for the rearrangement of 2h Na^+ (no ion swapping is required in this case) is probably also connected to a higher degree of variation for this disordered site.[40,53]

Ln^{3+}-doping induced disorder (Ln = Er, Tm, and Yb). The above discussion of the individual configurations of undoped β-$NaYF_4$ also applies largely to the doped versions of these configurations. As for the undoped lattice, configuration 10 was the energetically most stable one, irrespective of the Ln^{3+} dopant (Table S1†). It must be kept in mind though, that upon doping, configuration 10 is no longer identical to configuration 1 due to the exchange of one Y^{3+} by an Ln^{3+} at two differing positions in the supercell. The data obtained for configuration 1 and 10 (Table S1†) suggest that doping at the 1a site was minimally more favourable than at the 1f site ($\Delta E \approx$ 0.1 kJ mol^{-1}) for all three dopants. This is at odds with what Park *et al.* found in their study, reporting a stabilisation of approximately 1, 2, and 4 kJ mol^{-1} for Er^{3+}, Tm^{3+}, and Yb^{3+}, respectively, for doping at the 1f site (no exact values were given, and they were instead estimated from a figure provided in the publication).[52] Although the authors used a different methodology, model, and doping concentration, there is no apparent explanation for this discrepancy. Experimental measurements point to an equal occupation of the two sites (*i.e.*, 1a and 1f), inferring a rather small energetic difference, which supports our results.[27] Homologous to the undoped configurations, the doped versions were found to prefer configurations where Na^+ and Y^{3+} alternate regularly and no local clusters of either ion (configurations 7 to 13) are formed. Lattice energies and bond lengths for the doped configurations also mimicked their undoped counterparts as shown for configuration 10 in Table S1† and Table 7, respectively. Especially the reduction of bond lengths due to the lanthanide contraction was not as pronounced for two of the three investigated Ln^{3+} as observed in an earlier study.[49] A reduction of about 2.6% was observed for Yb^{3+}, compared to an expected value of 3.3%. Though, for Er^{3+} and Tm^{3+} almost no change was observed. A possible reason for this might be the almost identical ionic sizes of Er^{3+} and Tm^{3+}, compared to Y^{3+}, and the low doping percentage. Furthermore, when doping Er^{3+} into the three configurations with different 2h disorder (Table 6B), differences were overall minor. Changes from configuration to configuration were small and mostly followed the ones described for the undoped crystal.

Considering these results, for structures with a low doping concentration, the intrinsic disorder induced by the lattice itself seems to be far more influential than the disorder induced by the dopant ion. These findings contradict the statements of an earlier experimental study, which assumed severe structural changes induced by doping and how these changes explain why $P6_3/m$ is the more appropriate space group for β-$NaYF_4$.[42] While we do not argue whether $P6_3/m$ or $P\bar{6}$ is the more accurate designation, we would like to emphasise that the results obtained from the present study do not support the previously made hypothesis. Instead of arguing that doping will distort the lattice and thereby create different local environments for the dopant, it seems more appropriate that different dopant sites are created through the occupational

Table 7 Comparison of lattice energies relative to configuration 10 (ΔE), deviations of the lattice parameters ($Dev._{LP}$), and bond lengths (Y^{3+}–F^-) of configuration 10 for β-$NaYF_4$ doped with Er^{3+} (DZVP and TZV2P), Tm^{3+}, or Yb^{3+}

Ln^{3+}	ΔE (kJ mol^{-1})	$Dev._{LP}$ (%)	Y^{3+}–F^- (Å)
	β-$NaYF_4$: 4.2% Ln^{3+}		
—	—	0.77	2.338
Er^{3+}	0.00	0.76	2.338
Er^{3+}_{TZV2P}	−0.12	0.76	2.338
Tm^{3+}	—	0.76	2.338
Yb^{3+}	—	0.77	2.333

disorder of the lattice, and at these sites, ions can be doped into. This should be true for both space groups discussed for β-$NaYF_4$ but also α-$NaYF_4$ and related compounds. The earlier report even provides evidence for this explanation as it demonstrated that the local surrounding of the dopants does not change when increasing the dopant concentration from 0.5 to 20 mol%.

Lastly, one additional calculation for Er^{3+}-doped β-$NaYF_4$ in configuration 10 was conducted in which the basis set for Er^{3+} was expanded (TZV2P). This calculation was repeated with all other parameters kept constant. In principle, increasing the size of the basis set is expected to improve the reliability of the obtained results (on the expense of an increased computational demand). Compared to the results obtained with the smaller DZVP basis set, increasing the basis set reduced the energy of the supercell by 0.12 kJ mol^{-1}, and influenced the lattice parameters as well as the average positions of the nine F^- by about 0.1% (Table 7). Note that different to all other tables the reference value for ΔE in this table was not the lowest value displayed (*i.e.*, the TZV2P value) but the one from the DZVP calculation for better comparison with the energetic differences for the other Er^{3+}-doped configurations (*i.e.*, Table 4, Table S1† and Table 6). Hence, there was no indication that the overall trends observed will significantly change when recalculating all doped structures with this larger basis set on Ln^{3+}.

From infinite and defect-free computational crystal structures to nanoscale materials: potentials and limitations

While results obtained from computational studies undoubtedly provide valuable insights, their direct applicability to the properties of experimentally obtained (nano)materials may remain uncertain as a computational model always comes with inherent simplifications and assumptions not necessarily transferable to real life. This indeed holds also true for the here presented study. Hence, in light of this, the following considerations, including potential and limitations of the presented model, shall be kept in mind.

It is important to acknowledge that the synthesis of nanoparticles (but also bulk materials) inevitably induces a plethora of defects within the lattice and at the material's surface. In case of upconverting nanoparticles, these defects can influence the structural properties of the host material as well as the optical properties of the dopants.[80] Such deviations from the perfectly ordered, infinitely repeating unit cell that forms the basis of the computational approach become especially relevant for nanoparticles with their small volume-to-surface ratio. With a large share of unit cells close to the surface, lattice defects, dangling bonds, and the nanoparticle's environment become more and more relevant as particle size decreases. This constitutes a limitation of the model designed for this (and other) computational study as such surface effects cannot be easily assessed.

Most studies in the literature focus on the upconverting ions doped into inorganic host crystals. Conversely, the focus of this study explicitly lays on the lattice structure of the examined crystals and its disorder. Other groups computationally predicted the properties of dopant ions in crystals such as α- and β-$NaYF_4$.[28,49,52,81–84] Indeed, some of these studies appreciate differently induced disorder, yet, typically at a more shallow level. In most of these computational approaches, surface effects and transferability to the nanoscale remain unaddressed – an open question to be tackled in future works by the community.

A key challenge when setting up appropriate computational models is that defects are not necessarily distributed homogeneously across a nanoparticle but tend to accumulate near the surface.[85] On the other hand, the larger a nanoparticle the larger its portion that is sufficiently far away from the surface so that close-to-bulk properties may be assumed.[86] We would therefore argue that – except for the smallest nanoparticles – the chosen configurations become representative for most parts of a nanoparticle.

With these aspects in mind, the presented calculations are foreseen to act as stepping stone towards more realistic modelling at the nanoscale. While our model may still be closer to the bulk material than to a nanoparticle, it is arguably closer to the latter than the computational models previously designed. This is due to the fact that it incorporates disorder on a level much closer to experimentally obtained materials. Nevertheless, it is important to acknowledge that future work will have to consider effects of surface, disorder, and defects on the structure in general and dopant properties in particular at the nanoscale.

Conclusions

In this study, the atomistic structure of two model systems for photon upconverting crystals were investigated with density functional theory, namely the ordered crystal structure of $LiYF_4$ and the disordered structure of β-$NaYF_4$. Undoped as well as Er^{3+}-, Tm^{3+}-, or Yb^{3+}-doped crystals were created in the developed model, and the relative stability of different disordered atomistic arrangements was investigated. Results obtained from these systems were compared to already existing data when available to validate the model. Furthermore, new data were generated to answer questions about the effect of occupational disorder and disorder induced *via* doping into the crystal structure.

The results of this study can be best evaluated by dividing them into four categories. First, it was demonstrated that the chosen methodology (DFT with periodic boundary conditions) and programme (CP2K) are well suited for predicting atomistic properties of an ordered inorganic crystal structure, such as $LiYF_4$. We then verified the suitability of this model to predict crystal structures and to examine local variations for a disordered crystal, namely β-$NaYF_4$. Second, a rational for creating such a model was provided. It was found that a sufficiently large supercell of the crystal must be created, and a significant although not too extensive number of configurations must be assessed. These configurations must be chosen wisely so that

each represents one possible and ideally highly likely distribution of ions in the disordered lattice. Third, in the case of β-$NaYF_4$, three potential sources of variations within the crystal were examined: disordered 1f sites, disordered 2h sites, and disorder induced through doping with Er^{3+}, Tm^{3+}, or Yb^{3+}. Of these three possible sources of disorder, disordered 1f and 2h sites were identified as those that most significantly influence the positions of the F^- ions around potential doping sites. While changes at 1f sites seemed to be more relevant than those at 2h sites, both were found to be much more important than changes introduced by low-concentration doping. In general, low-percentage doping does not appear to be a significant source of distortion for these crystal structures. Forth and finally, assumptions of earlier studies focusing on the 1f disorder (alternating rows of Na^+ and Y^{3+}) were mostly confirmed but more importantly also refined. After all, the X-ray structural information of β-$NaYF_4$ is in line with the results of our protocol (once averaged over the different configurations) and the crystal structure should be considered as being significantly disordered.

In summary, this study showed the high likelihood that the β-$NaXF_4$ (X = lanthanides plus yttrium) crystal family is best described as consisting of a variety of unit cells, all with differing configurations of the ionic positions. The knowledge gained about the local variations of ions around potential doping sites can act as stepping stone for future studies to more accurately predict properties such as energy levels and energy gaps of individual Ln^{3+} or oscillator strengths and energy transfer rates between pairs of dopants in these crystals. Ultimately, this may lead to the design of next-generation upconverting nanoparticles overcoming current limitations such as low quantum yield.

Author contributions

Chris Steve Conrad: investigation, formal analysis, writing – original draft, conceptualization (general project, approach, model setup), funding acquisition; Holger Euchner: investigation, conceptualisation (theoretical approach), writing – review and editing; Eva Hemmer: conceptualisation (underlying goal and compound selection), writing – review and editing, supervision; Reinhold F. Fink: conceptualisation (approach, model setup), writing – review and editing, supervision, funding, resources.

Data availability

The optimised crystal structures of $LiYF_4$ and of configuration 10 of undoped β-$NaYF_4$ are provided in the ESI.† All other are available from the authors upon request or at **https://doi.org/10.6084/m9.figshare.27846741.v1**.

Conflicts of interest

There are no conflicts to declare.

Acknowledgements

CSC is grateful for a scholarship by Friedrich-Ebert-Stiftung and support from MITACS. CSC and RFF acknowledge support by the state of Baden-Württemberg through bwHPC and the German Research Foundation (DFG) through grant no INST 40/575-1 FUGG (JUSTUS 2 cluster). EH acknowledges the Natural Sciences and Engineering Research Council of Canada (NSERC RGPIN-2023-03985). Images shown in the ToC figure were partially made in BioRender (**https://www.biorender.com**).

References

1 F. Auzel, *C. R. Acad. Sci.*, 1966, **262**, 1016.
2 F. Auzel, *C. R. Acad. Sci.*, 1966, **263**, 819.
3 F. Auzel, *Chem. Rev.*, 2004, **104**, 139–174.
4 S. Heer, O. Lehmann, M. Haase and H.-U. Güdel, *Angew. Chem., Int. Ed.*, 2003, **42**, 3179–3182.
5 M. Haase and H. Schäfer, *Angew. Chem., Int. Ed.*, 2011, **50**, 5808–5829.
6 S. Qiao, R. Pu, X. Guo, Y. Ni, C. Wu, B. Wang, Y. Du, J. Huang, K. Zheng, W. Wei and Q. Zhan, *ACS Appl. Nano Mater.*, 2024, **7**, 12795–12805.
7 R. S. Ajee, P. S. Roy, S. Dey and S. Sundaresan, *J. Nanopart. Res.*, 2024, **26**, 50.
8 S. Varghese, A. S. Madanan, M. K. Abraham, A. I. Shkhair, G. Indongo, G. Rajeevan, B. K. Arathy and S. George, *Microchem. J.*, 2024, **206**, 111539.
9 M. Liu, J. Liang and F. Vetrone, *Acc. Chem. Res.*, 2024, **57**, 2653–2664.
10 J. Y. Jung, J. Y. Park and H. K. Yang, *Adv. Opt. Mater.*, 2024, **12**, 2401210.
11 Z. Fan, Y. Shao, X. Jiang, J. Zhou, L. Yang, H. Chen and W. Liu, *Int. J. Biol. Macromol.*, 2024, **278**, 134187.
12 Y. Yang, K. Q. Long, Y. X. Chu, H. P. Lu, W. P. Wang and C. Y. Zhan, *Adv. Funct. Mater.*, 2024, **34**, 2402975.
13 Y. Jiang, Y. Hong, Y.-Y. Liu, Y. Guan, J. Zhou, H. Wang and L. Sun, *J. Mater. Chem. C*, 2024, **12**, 11938–11947.
14 C. Xu, S. K. Law and A. W. N. Leung, *Pharmaceuticals*, 2024, **17**, 663.
15 M. Hosseinifard, N. Jurga, J. C. Brandmeier, Z. Farka, A. Hlaváček, H. H. Gorris, T. Grzyb and A. Ekner-Grzyb, *Chemosphere*, 2024, **347**, 140629.
16 J. Yu, H. Yu, L. Li, X. Ni, K. Song and L. Wang, *ChemNanoMat*, 2021, **7**, 859–872.
17 A. Alotaibi, F. Alsardi, F. Alshwikhat, M. Aldossary, F. S. Almarwani, F. J. Talidi, S. A. Almenhali, S. F. Almotawa, Y. A. Alzahrani, S. Alenzi, A. Alanazi and M. Alkahtani, *Molecules*, 2024, **29**, 2556.
18 W. Zhang, W. Zheng, P. Huang, D. Yang, Z. Shao and X. Chen, *Aggregate*, 2024, **5**, e558.
19 N. Dubey and S. Chandra, *J. Rare Earths*, 2022, **40**, 1343–1359.
20 A. A. Ansari, M. A. M. Khan, B. P. Singh and A. K. Parchur, *J. Mater. Sci.: Mater. Electron.*, 2023, **34**, 1625.

21 S. Mohanty and A. M. Kaczmarek, *Chem. Soc. Rev.*, 2022, **51**, 6893–6908.
22 X. Xia, E. Sivonxay, B. A. Helms, S. M. Blau and E. M. Chan, *Nano Lett.*, 2023, **23**, 11129–11136.
23 F. Li, L. Tu, Y. Zhang, D. Huang, X. Liu, X. Zhang, J. Du, R. Fan, C. Yang, K. W. Krämer, J. Marques-Hueso and G. Chen, *Nat. Photonics*, 2024, **18**, 440–449.
24 C. K. J. Renata Reisfeld, *Lasers and Excited States of Rare Earths*, Springer-Verlag, Berlin Heidelberg New York, 1977.
25 R. Renata, *AIMS Mater. Sci.*, 2015, **2**, 37–60.
26 W. T. Carnall, in *Handbook on the Physics and Chemistry of Rare Earths*, ed. K. A. Gschneidner and L. Eyring, North-Holland Publishing Company, Amsterdam, 1979, vol. 3, ch. 24, p. 171–208.
27 A. Aebischer, M. Hostettler, J. Hauser, K. Krämer, T. Weber, H. U. Güdel and H.-B. Bürgi, *Angew. Chem., Int. Ed.*, 2006, **45**, 2802–2806.
28 A. Platonenko and A. I. Popov, *Opt. Mater.*, 2020, **99**, 109529.
29 X. Zhu, J. Zhang, J. Liu and Y. Zhang, *Adv. Sci.*, 2019, **6**, 1901358.
30 Y. Wu, M. J. Y. Ang, M. Sun, B. Huang and X. Liu, *J. Phys. D: Appl. Phys.*, 2019, **52**, 383002.
31 R. Shannon, *Acta Crystallogr., Sect. A*, 1976, **32**, 751–767.
32 I. Halimi, E. M. Rodrigues, S. L. Maurizio, H.-Q. T. Sun, M. Grewal, E. M. Boase, N. Liu, R. Marin and E. Hemmer, *J. Mater. Chem. C*, 2019, **7**, 15364–15374.
33 C. Homann, N. Liu, H. Barbosa and E. Hemmer, in *Handbook on the Physics and Chemistry of Rare Earths*, ed. J.-C. G. Bünzli and S. M. Kauzlarich, Elsevier, 2024, vol. 65, pp. 137–212.
34 J. F. Suyver, J. Grimm, M. K. van Veen, D. Biner, K. W. Krämer and H. U. Güdel, *J. Lumin.*, 2006, **117**, 1–12.
35 C. Renero-Lecuna, R. Martín-Rodríguez, R. Valiente, J. González, F. Rodríguez, K. W. Krämer and H. U. Güdel, *Chem. Mater.*, 2011, **23**, 3442–3448.
36 D. Pominova, V. Proydakova, I. Romanishkin, S. Kuznetsov, K. Linkov, N. Tabachkova and A. Ryabova, *Photonics*, 2024, **11**, 38.
37 S. Han, R. Deng, X. Xie and X. Liu, *Angew. Chem., Int. Ed.*, 2014, **53**, 11702–11715.
38 L. D. DeLoach, S. A. Payne, L. L. Chase, L. K. Smith, W. L. Kway and W. F. Krupke, *IEEE J. Quantum Electron.*, 1993, **29**, 1179–1191.
39 G. Blasse and B. C. Grabmaier, *Luminescent Materials*, Springer, Berlin, 1994, pp. 123.
40 R. Shi, C. D. S. Brites and L. D. Carlos, *Nanoscale*, 2021, **13**, 19771–19782.
41 P. Pandey, S. D. Kaushik, P. Rajput, M. N. Singh, R. K. Sharma and S. Giri, *Nanoscale*, 2025, **17**, 2269–2280.
42 D. Tu, Y. Liu, H. Zhu, R. Li, L. Liu and X. Chen, *Angew. Chem., Int. Ed.*, 2013, **52**, 1128–1133.
43 J. H. Burns, *Inorg. Chem.*, 1965, **4**, 881–886.
44 R. E. Thoma, H. Insley and G. M. Hebert, *Inorg. Chem.*, 1966, **5**, 1222–1229.
45 D. M. Roy and R. Roy, *J. Electrochem. Soc.*, 1964, **111**, 421.
46 K. W. Krämer, D. Biner, G. Frei, H. U. Güdel, M. P. Hehlen and S. R. Lüthi, *Chem. Mater.*, 2004, **16**, 1244–1251.
47 A. A. Bunaciu, E. G. Udriștioiu and H. Y. Aboul-Enein, *Crit. Rev. Anal. Chem.*, 2015, **45**, 289–299.
48 G. Yao, M. T. Berry, P. S. May and D. S. Kilin, *Int. J. Quantum Chem.*, 2012, **112**, 3889–3895.
49 G. Yao, M. T. Berry, P. S. May and D. Kilin, *J. Phys. Chem. C*, 2013, **117**, 17177–17185.
50 G. Yao, M. Berry, P. S. May, J. Wang and D. S. Kilin, *J. Phys. Chem. C*, 2016, **120**, 7785–7794.
51 F. Wang, Y. Han, C. S. Lim, Y. Lu, J. Wang, J. Xu, H. Chen, C. Zhang, M. Hong and X. Liu, *Nature*, 2010, **463**, 1061–1065.
52 K.-W. Park, H. S. Jang and S.-H. Cho, *Mater. Chem. Phys.*, 2022, **275**, 125317.
53 B. Szefczyk, R. Roszak and S. Roszak, *RSC Adv.*, 2014, **4**, 22526–22535.
54 B. Huang, H. Dong, K.-L. Wong, L.-D. Sun and C.-H. Yan, *J. Phys. Chem. C*, 2016, **120**, 18858–18870.
55 B. P. Sobolev, D. A. Mineev and V. Pashutin, *Dokl. Akad. Nauk SSSR*, 1963, **150**, 791–794.
56 A. Grzechnik and K. Friese, *Dalton Trans.*, 2012, **41**, 10258–10266.
57 R. E. Thoma, C. F. Weaver, H. A. Friedman, H. Insley, L. A. Harris and H. A. Yakel Jr, *J. Phys. Chem.*, 1961, **65**, 1096–1099.
58 V. T. Vera, D. Mendez-Gonzalez, D. J. Ramos-Ramos, A. Igalla, M. Laurenti, R. Contreras-Caceres, E. Lopez-Cabarcos, E. Díaz, J. Rubio-Retama, S. Melle and O. G. Calderón, *J. Mater. Chem. C*, 2021, **9**, 8902–8911.
59 R. Joshi, R. S. Perala, S. B. Shelar, A. Ballal, B. P. Singh and R. S. Ningthoujam, *ACS Appl. Mater. Interfaces*, 2021, **13**, 3481–3490.
60 J. Hutter, M. Iannuzzi, F. Schiffmann and J. VandeVondele, *Wiley Interdiscip. Rev.:Comput. Mol. Sci.*, 2014, **4**, 15–25.
61 G. Lippert, J. Hutter and M. Parrinello, *Mol. Phys.*, 1997, **92**, 477–488.
62 J. VandeVondele, M. Krack, F. Mohamed, M. Parrinello, T. Chassaing and J. Hutter, *Comput. Phys. Commun.*, 2005, **167**, 103–128.
63 J. Vande Vondele and J. Hutter, *J. Chem. Phys.*, 2003, **118**, 4365–4369.
64 J. VandeVondele and J. Hutter, *J. Chem. Phys.*, 2007, **127**, 114105.
65 S. Goedecker, M. Teter and J. Hutter, *Phys. Rev. B:Condens. Matter Mater. Phys.*, 1996, **54**, 1703–1710.
66 J. P. Perdew, K. Burke and M. Ernzerhof, *Phys. Rev. Lett.*, 1996, **77**, 3865–3868.
67 S. Grimme, J. Antony, S. Ehrlich and H. Krieg, *J. Chem. Phys.*, 2010, **132**, 154104.
68 K. Momma and F. Izumi, *J. Appl. Crystallogr.*, 2011, **44**, 1272–1276.
69 C. Keller and H. Schmutz, *J. Inorg. Nucl. Chem.*, 1965, **27**, 900–901.
70 W. Y. Ching, Y.-N. Xu and B. K. Brickeen, *Phys. Rev. B: Condens. Matter Mater. Phys.*, 2001, **63**, 115101.

71 M. V. Luong, M. J. F. Empizo, J. L. F. Gabayno, Y. Minami, K. Yamanoi, T. Shimizu, N. Sarukura, M. H. Pham, H. D. Nguyen, K. G. Steenbergen, P. Schwerdtfeger and M. Cadatal-Raduban, *Comput. Mater. Sci.*, 2018, **153**, 431–437.
72 E. Garcia and R. R. Ryan, *Acta Crystallogr., Sect. C:Cryst. Struct. Commun.*, 1993, **49**, 2053–2054.
73 J. Yin, Q. Zhang, T. Liu, X. Guo, M. Song, X. Wang and H. Zhang, *Nucl. Instrum. Methods Phys. Res., Sect. B*, 2009, **267**, 74–78.
74 S. Li, R. Ahuja and B. Johansson, *J. Phys.: Condens. Matter*, 2004, **16**, 983.
75 J. P. Perdew, *Phys. Rev. B:Condens. Matter Mater. Phys.*, 1986, **33**, 8822–8824.
76 R. Moncorgé, in *Ultraviolet Spectroscopy and UV Lasers*, ed. M. A. D. P. Misra, Marcel Dekker Inc., New York, Basel, 2005, pp. 337–370.
77 Á. Morales-García, R. Valero and F. Illas, *J. Phys. Chem. C*, 2017, **121**, 18862–18866.
78 K. Chong, T. Hirai, T. Kawai, S. Hashimoto and N. Ohno, *J. Lumin.*, 2007, **122–123**, 149–151.
79 H. Sato and R. Kikuchi, *J. Chem. Phys.*, 1971, **55**, 677–702.
80 P. Rudolph, *Prog. Cryst. Growth Charact. Mater.*, 2016, **62**, 89–110.
81 Y. Han, D. J. Vogel, T. M. Inerbaev, P. S. May, M. T. Berry and D. S. Kilin, *Mol. Phys.*, 2018, **116**, 697–707.
82 C. M. S. Calado, Í.F Manali, I. M. S. Diogenis, S. F. N. Coelho, V. C. Teixeira, B. R. de Mesquita, J. L. Oliveira, F. A. Sigoli and M. V. D. S. Rezende, *Opt. Mater.*, 2023, **137**, 113529.
83 X. Qin and X. Liu, *Nanoscale*, 2021, **13**, 19561–19567.
84 X. Qin, L. Shen, L. Liang, S. Han, Z. Yi and X. Liu, *J. Phys. Chem. C*, 2019, **123**, 11151–11161.
85 G. Tessitore, G. A. Mandl, M. G. Brik, W. Park and J. A. Capobianco, *Nanoscale*, 2019, **11**, 12015–12029.
86 M. Quintanilla, E. Hemmer, J. Marques-Hueso, S. Rohani, G. Lucchini, M. Wang, R. R. Zamani, V. Roddatis, A. Speghini, B. S. Richards and F. Vetrone, *Nanoscale*, 2022, **14**, 1492–1504.